Towards *in vivo* imaging of intramolecular fluorescence resonance energy transfer parameters

Vaibhav Gaind,[1] Kevin J. Webb,[1,*] Sumith Kularatne,[2] and Charles A. Bouman[1]

[1]*School of Electrical and Computer Engineering, Purdue University, 465 Northwestern Avenue, West Lafayette, Indiana 47907, USA*
[2]*Department of Chemistry, 560 Oval Drive, West Lafayette, Indiana 47907-2084, USA*
[*]*Corresponding author: webb@purdue.edu*

Received December 2, 2008; revised April 20, 2009; accepted May 13, 2009;
posted May 18, 2009 (Doc. ID 104722); published July 15, 2009

Fluorescence resonance energy transfer (FRET) is a nonradiative energy transfer process based on dipole-dipole interaction between donor and acceptor fluorophores that are spatially separated by a distance of a few nanometers. FRET has proved to be of immense value in the study of cellular function and the underlying cause of disease due to, for example, protein misfolding (of consequence in Alzheimer's disease). The standard parameterization in intramolecular FRET is the lifetime and yield, which can be related to the donor-acceptor (DA) distance. FRET imaging has thus far been limited to *in vitro* or near-surface microscopy because of the deleterious effects of substantial scatter. We show that it is possible to extract the microscopic FRET parameters in a highly scattering environment by incorporating the FRET kinetics of an ensemble of DA molecules connected by a flexible or rigid linker into an optical diffusion tomography (ODT) framework. We demonstrate the efficacy of our approach for extracting the microscopic DA distance through simulations and an experiment using a phantom with scattering properties similar to tissue. Our method will allow the in vivo imaging of FRET parameters in deep tissue, and hence provide a new vehicle for the fundamental study of disease.
© 2009 Optical Society of America
OCIS codes: 170.3880, 170.3660, 170.6960, 100.3190.

1. INTRODUCTION

Fluorescence resonance energy transfer (FRET) results in a decrease in the lifetime and quantum yield of the donor in the presence of the acceptor [1,2]. Both intramolecular and intermolecular FRET have been extensively used in the *in vitro* study of molecular activity related to cellular function and the cause of disease [3–9]. In intramolecular FRET, the donor and acceptor are connected by a linker and energy transfer is between a single donor and acceptor (fixed stoichiometry). The donor-acceptor (DA) distance is fixed for a rigid linker or is distributed over some (nm) range for a flexible linker [2]. Intramolecular FRET has been used to study protease activity [3], conformational changes in proteins [4], protein phosphorylation [5], biological phenomena like protein folding and denaturation [2,8], and to measure intracellular calcium [6]. The study of protein folding and aggregation by FRET could be important in relation to diseases like Alzheimer's and some cancers which have been linked to protein misfolding [10,11]. In intermolecular FRET, the donor and acceptor reside on independent unlinked hosts and, therefore, there can be multiple acceptors for a single donor. Intermolecular FRET has been used to study protein-protein interactions [7].

The deleterious effects of substantial scatter precludes the direct imaging of molecular activity using FRET in deep tissue. Until now, the imaging of FRET in tissue has been limited to surgically removed thin tissue sections [12,13] and near surface *in vivo* [14] multiphoton microscopy. While multiphoton or confocal microscopy allows the spatial mapping of FRET parameters [13], this is limited to weak scatter. Optical diffusion tomography (ODT), where the propagation of light in a scattering medium is modeled by a diffusion equation, facilitates deep tissue imaging [15,16]. With the appropriate data set, ODT has been used to image fluorescence yield and lifetime [17]. Combining ODT with FRET would thus enable three-dimensional spatial mapping of FRET parameters and allow *in-vivo* deep-tissue imaging of molecular activity indicated by the microscopic DA distance or distance distribution.

Molecular beacons (MBs) [18] are similar in construction to FRET molecules, as they have a fluorophore linked to a quencher, and *in-vivo* images have been achieved for a mouse model [19] using techniques similar to fluorescence optical diffusion tomography (FODT) [17]. However, due to their particular construction, in which the fluorophore-quencher distance in MBs is much less than the DA distance in FRET probes, MBs behave fundamentally differently [20,21] and provide no distance information.

We describe an approach to couple the kinetics of intramolecular FRET, with a rigid or flexible linker, with a model that describes multiply scattered light, thereby allowing the estimation of the microscopic FRET distance or distance distribution inside a scattering medium. To describe the light scatter, we use a diffusion model, which is valid at length scales large relative to the photon randomization length $l_s=(3D)^{-1}$, where D is the diffusion coefficient, which in tissue is on the millimeter scale. Therefore, ODT length scales are not commensurate with FRET DA distances, making it unclear whether it would be pos-

sible to determine the DA distance from heavily scattered light. Combining FRET and ODT requires that we have an ensemble of DA pairs in order to ensure an adequate detector signal to noise ratio (SNR). Through simulations and a simple experiment, we show that it is possible to determine the microscopic FRET parameters. Specifically, the DA distance or distance distribution for rigid or flexible linkers, respectively, is reconstructed using the macroscopic ODT modality.

2. FRET-ODT PARAMETERIZATION

In the excited state and in the presence of an acceptor, the donor molecule can decay to the ground state radiatively by photon emission with rate k_r and non-radiatively, by heat dissipation and energy transfer to an acceptor molecule, with rates k_{nr} and k_F, respectively [1,2]. If τ_D is the donor lifetime and η_D the donor quantum yield in the absence of an acceptor, then $k_F=\tau_D^{-1}(R_0/r_F)^6$, where r_F is the distance between the donor and the acceptor and R_0 is the DA distance where the energy transfer efficiency is 50%, $\tau_D^{-1}=k_r+k_{nr}$, and $\eta_D=k_r/(k_r+k_{nr})$ [2]. In the presence of an acceptor, energy transfer results in a decreased donor lifetime, τ_{DA}, given by

$$\frac{1}{\tau_{DA}}=\frac{1}{\tau_D}\left[1+\left(\frac{R_0}{r_F}\right)^6\right]=k_r+k_{nr}+k_F \tag{1}$$

and a decreased donor quantum yield

$$\eta_{DA}=\frac{k_r}{k_r+k_{nr}+k_F}. \tag{2}$$

For an ensemble of flexible linkers, the DA distance is commonly modeled by a probability distribution, which we assume to be Gaussian within the distance range $[r_{min},r_{max}]$ and given by $p(r_F)=(1/Z)\exp\{-a(r_F-b)^2\}$, where $Z=\int_{r_{min}}^{r_{max}}\exp\{-a(r_F-b)^2\}dr_F$ is the partition function, b is the mean DA distance, and a is inversely proportional to the variance [2,8].

For an ensemble of DA pairs connected by flexible linkers, in a highly scattering medium, we model the excitation and donor fluorescence photon propagation by the frequency domain coupled diffusion equations [17,22]

$$\nabla\cdot[D_x(r)\,\nabla\,\varphi_x(r,\omega)]-[\mu_{ax}(r)-i\omega/c]\varphi_x(r,\omega)=-S_x(r;\omega) \tag{3}$$

$$\nabla\cdot[D_m(r)\,\nabla\,\varphi_m(r,\omega)]-[\mu_{am}(r)-i\omega/c]\varphi_m(r,\omega)=-\varphi_x(r,\omega)S_f(r;\omega), \tag{4}$$

with $\exp(-i\omega t)$ time dependence and circular modulation frequency ω (rad s^{-1}), where subscripts x and m, respectively, denote the excitation and emission wavelengths λ_x and λ_m, $\varphi(r,\omega)$ (W cm^{-2}) is the photon flux density at position r inside the scattering medium, a point source $S_x(r;\omega)=\beta\delta(r-s)$ is assumed, with β the modulation depth, c is the speed of light in the medium, $\mu_a(r)$ (cm^{-1}) is the absorption coefficient at position r, $D(r)$ (cm) is the diffusion coefficient at position r, and $S_f(r,\omega)$ is the source for the flexible (subscript f) linker. Using the Fourier transform of the time-domain impulse response of the donor fluorophore, $[(\eta_{DA}.\mu_{aD})/\tau_{DA}].\exp(-t/\tau_{DA})$, along with (1) and (2),

$$S_f(r;\omega)=\int_{r_{min}}^{r_{max}}\frac{\eta_{DA}\mu_{aD}(r)}{1-i\omega\tau_{DA}(r)}p(r_F(r))\mathrm{d}r_F(r)=\int_{r_{min}}^{r_{max}}\eta(r)\zeta(r_F(r))p(r_F(r))\mathrm{d}r_F(r), \tag{5}$$

upon setting $\eta_{DA}=k_r\tau_{DA}$ and $\eta_D=k_r\tau_D$, where the distance-dependent τ_{DA} and η_{DA} are averaged over DA distance r_F using the distribution $p(r_F)$, $\zeta(r_F(r))=r_F^6(r).[(1-i\omega\tau_D(r))r_F^6(r)+R_0^6]^{-1}$, $r_F(r)$ is the DA distance at point r, $\mu_{aD}(r)$ is the absorption coefficient of the donor, and for notational simplicity, $\eta(r)=\eta_D\mu_{aD}(r)$. Modulated light is necessary to determine all parameters in (5). For an ensemble of DA pairs connected by rigid linkers, $p(r_F)$ reduces to a Dirac delta function, and the corresponding source term is $S_g(r;\omega)=\eta(r)\zeta(r_F(r))$, where the subscript g indicates a rigid linker. We chose the DA distance and distance distribution to parameterize the FRET image, rather than donor lifetime in presence of the acceptor, τ_{DA}, because distance is a natural measure for FRET and, for the flexible linker, the probability distribution is Gaussian if the FRET image is parameterized in terms of distance, while for τ_{DA}, the distribution would be non-Gaussian. Having a Gaussian distribution makes it easier to calculate the integral in (5). Let $g_x(r_{s_k},r;\omega)$ be the diffusion equation Green's function for (3) at wavelength λ_x and $g_m(r,r_{d_m};\omega)$ be the Green's function for (4) at λ_m. Then, the donor fluorescence photon flux density (for flexible or rigid linker) at a detector positioned at r_{d_m}, due to a point source modulated at frequency ω and positioned at r_{s_k}, is

$$\varphi(r_{s_k},r_{d_m};\omega)=\int g_m(r,r_{d_m};\omega)S(r;\omega)g_x(r_{s_k},r;\omega)\mathrm{d}^3r, \tag{6}$$

where $S(\cdot)$ represents either S_f or S_g.

Assuming that μ_{a_x}, D_x, μ_{a_m}, D_m, and τ_D are known or have been reconstructed using a procedure we have previously described [17], then, for the flexible linker, the unknown parameters can be represented as $x_F=[\eta(r),a(r),b(r)]^T$, or for the rigid linker as $x_F=[\eta(r),r_F(r)]^T$, where T is transpose. We use K optical sources modulated at Q frequencies for excitation and M detectors to measure the emitted donor fluorescence. To reconstruct x_F and thus locate the ensemble inside the scattering medium, the measurements are incorporated in a Bayesian framework [17,23], which facilitates a statistical approach for the reconstruction of x_F.

3. RECONSTRUCTION

To reconstruct x_F, the simulation domain is discretized into N nodes on a uniform 3-D grid, which transformed x_F into the $3N\times1$ vector

$$x_F=[\eta(r_1)\cdots\eta(r_N),a(r_1)\cdots a(r_N),b(r_1)\cdots b(r_N)]^T \tag{7}$$

for the flexible linker, and the $2N\times1$ vector

$$x_F = [\eta(r_1)\cdots\eta(r_N), r_F(r_1)\cdots r_F(r_N)]^T \quad (8)$$

for the rigid linker, where the superscript T denotes the transpose operation.

Source and detector calibration coefficients [24] are explicitly introduced into the inversion. The inversion problem is couched in a Bayesian framework [17,23], which allows us to incorporate *a priori* information as well as information about the physics of the FRET model into the maximum *a posteriori* (MAP) estimate

$$\{\hat{x}_F\}_{MAP} = \arg\max_{x_F \geq 0, s, d} \left\{ \prod_{q=1}^{Q} p(y_{F_q}|x_F, s_q, d_q) p(x_F) \right\}, \quad (9)$$

where $p(y_{F_q}|x_F, s_q, d_q)$ is the data likelihood for the fluorescence signal measured from an ensemble of DA pairs connected by either flexible or rigid linker located inside a scattering medium, $p(x_F)$ is the prior model, y_{F_q} is a $KM \times 1$ vector representing the measurement at M detectors due to K sources modulated at frequency ω_q, Q denotes the total number of modulation frequencies, and $s_q = [s_{1_q}, \ldots s_{K_q}]$ and $d_q = [d_{1_q}, \ldots d_{M_q}]$ are the source and detector coupling coefficient vectors respectively, at frequency ω_q, for the K sources and M detectors, which are estimated jointly with the image x_F. For the simulations presented in the paper, $s_k = 1 + i0$ and $d_m = 1 + i0$ are used. Assuming a Gaussian shot-noise model, the data term is

$$p(y_{F_q}|x_F, s_q, d_q) = \frac{1}{(\pi\alpha_F)^P |\Lambda_{F_q}|^{-1}} \times \exp\left[- \frac{\|y_{F_q} - f_{F_q}(x_F, s_q, d_q)\|^2_{\Lambda_{F_q}}}{\alpha_F} \right], \quad (10)$$

where $P = KM$ is the number of measurements, $f_{F_q}(x_F)$ is a $KM \times 1$ vector of the form

$$f_{F_q}(x_F, s_q, d_q) = [s_{1_q} d_{1_q} \varphi(r_{s_1}, r_{d_1}; \omega, x_F) \ldots s_{1_q} d_{M_q} \times \varphi(r_{s_1}, r_{d_M}; \omega, x_F), s_{2_q} d_{1_q} \varphi(r_{s_2}, r_{d_1}; \omega, x_F) \ldots s_{K_q} d_{M_q} \varphi(r_{s_K}, r_{d_M}; \omega, x_F)]^T, \quad (11)$$

α_F is a scalar parameter that scales the noise variance, and, for an arbitrary vector w, $\|w\|^2_\Lambda = w^H \Lambda w$ (where H denotes Hermitian transpose), with $\alpha_F/(2\Lambda_{F_q}{}^{-1})$ the covariance matrix. We assume a shot noise model with $\Lambda_{F_q}{}^{-1} = \mathrm{diag}[|y_{F_q 1}|, \ldots |y_{F_q P}|]$ [23]. For the flexible linker, the prior density, $p(x_F)$, assuming independence of the image vectors representing η, a or b, is $p(x_F) = p(x_\eta).p(x_a).p(x_b)$. We use the generalized Gaussian Markov random field (GGMRF) prior [23]

$$p(x_k) = \frac{1}{\sigma_k^N z(\rho_k)} \exp\left(- \frac{1}{\rho_k \sigma^{\rho_k}} \sum_{\{i,j\} \in \mathcal{N}_k} b_{i-j} |x_{k_i} - x_{k_j}|^{\rho_k} \right), \quad (12)$$

where k represents η, a or b, x_{k_i} denotes the ith node of x_k, the set $\mathcal{N}_k$ consists of all pairs of neighboring nodes (in a 26 neighbor system), and b_{i-j} is the weighting coefficient corresponding to the ith and jth nodes assigned to be inversely proportional to the node separation, under the condition that $\Sigma_j b_{i-j} = 1$. Parameters ρ (we use $\rho_k = 2$) and σ control the shape and scale of the distribution and $z(\rho)$ normalizes the density. The prior model for the rigid linker can be described in a similar way.

Numerically, $\varphi(r_{s_k}, r_{d_m}; \omega, x_F)$ is calculated by discretizing (6), with $S(\cdot)$ being either S_f or S_g, as

$$\varphi(r_{s_k}, r_{d_m}; \omega, x_F) = \sum_{j=1}^{N} V[g_m(r_j, r_{d_m}; \omega) S(r_j; \omega, x_F) g_x(r_{s_k}, r_j; \omega)], \quad (13)$$

where V is the (cubic) element volume associated with each node and the dependence of the FRET source term, S, on the image x_F, is explicitly included by representing it as $S(r_j; \omega, x_F)$. Using (13), we rewrite (11) as

$$f_{F_q}(x_F, s_q, d_q) = G_{\omega_q} S_{\omega_q}(x_F), \quad (14)$$

which is the product of a $KM \times N$ matrix and a $N \times 1$ vector, with $G^{ij}_{\omega_q} = s_{k_q} d_{m_q} g_x(r_{s_k}, r_j; \omega_q).g_m(r_j, r_{d_m}; \omega_q)$, $m = i$ modulo M and $k = [i/M + 1]$, where [.] is the integer part of $i/M + 1$, and $S_{\omega_q}(x_F) = [S(r_1; \omega_q, x_F) \cdots S(r_N; \omega_q, x_F)]^T$. Previously, we found that incorporating α_F into the inverse problem as an unknown for each image tends to improve the robustness and speed of convergence [25]. As a result, we obtain the MAP estimate, $\{\hat{x}_F\}_{MAP}$, by performing a joint iterative minimization of $\ln[p(y_F|x_F)p(x_F)]$ over α_F, s_q, d_q and x_F, leading to

$$(\{\hat{x}_F\}_{MAP}, \hat{\alpha}_F, \hat{s}, \hat{d}) = \arg\min_{x_F \geq 0, s, d} \min_{\alpha_F} \left\{ \frac{1}{\alpha_F} \sum_{q=1}^{Q} \|y_{F_q} - G_{\omega_q} S_{\omega_q}(x_F)\|^2_{\Lambda_{F_q}} + P \log \alpha_F - \log[p(x_F)] \right\}. \quad (15)$$

As in our previous work, we use the iterative coordinate descent (ICD) algorithm, a Gauss-Seidel approach, along with a Golden Section Search, to estimate $\{\hat{x}_F\}_{MAP}$ from (15) [22]. In ICD, the cost function in (15) is optimized with respect to individual nodes in the image, where the image points are scanned in random order. For example, for the flexible linker, one update scan for x_F consisted of updating all N nodes first with respect to a, then b and subsequently η. For the flexible linker, with all other image elements fixed, the ICD update for the ith node in the image of a, b or η is

$$\hat{x}_{k_i} \leftarrow \arg\min_{x_{k_i} \geq 0} \left\{ \frac{1}{\hat{\alpha}_F} \sum_{q=1}^{Q} \|y_{F_q} - [G_{\omega_q}]_{*(i)} S(r_i; \omega_q, x_F)\|^2_{\Lambda_{F_q}} + \frac{1}{\rho_k \sigma_k^{\rho_k}} \sum_{j \in \mathcal{N}_{k_i}} b_{i-j} |x_{k_i} - \hat{x}_{k_j}|^{\rho_k} \right\}, \quad (16)$$

where $\leftarrow$ implies update, k represents either a, b or η, $\mathcal{N}_{k_i}$ is the set of nodes neighboring node i, and $[G_{\omega_q}]_{*(i)}$ denotes the ith column of G_{ω_q}.

4. SIMULATION

The model problem we consider is the cubical tissue phantom of Fig. 1(a) with side 2.5 cm, discretized on a $33\times33\times33$ uniform grid. A planar arrangement of 14 sources, with ten equally spaced modulation frequencies between 40 and 220 MHz (20 MHz between measurements), is on the top face and 14 detectors are used on the bottom face. The molecules EYFP and HcRED1 are assumed as donor and acceptor, respectively, with $\tau_D=3.8$ ns [26], and we use $R_0=4.7$ nm [27]. We assume $D_x\approx D_m=0.027$ cm and $\mu_{ax}\approx\mu_{am}=0.047$ cm^{-1}. For both rigid and flexible linker, we choose $\eta=0.025$ cm^{-1}, calculated from the quantum yield and absorption coefficient for EYFP, assuming a concentration of 250 nM for the FRET pair. The FRET pairs are contained within a centrally located sphere of radius 2.5 mm. We assume a FRET molecular concentration that is based on related work with a mouse tumor model [19], and tissue parameters for the light [16]. The detectors are assumed to be shot noise limited with an average SNR of 30 dB. We used MUDPACK to generate the synthetic data [28,29].

A. Computation of Equation (5)

Determining $\{\hat{x}_F\}_{MAP}$ involved multiple computations of the integral in (5). For given R_0, ω and τ_D, piecewise fitting cubic polynomials and exponential functions to the real and imaginary parts of $\zeta(r_F)$ leads to analytical expressions for the integral in (5). This provided an efficient way to parameterize the FRET source. The limits of integration in (5) were chosen to be $r_{min}=5$ Å and $r_{max}=3.5R_0$. The accuracy of this approach is illustrated in Fig. 2.

B. Simulation Results

Figure 1(b) shows the central slice of the discretized sphere (the isosurface plot in Fig. 1(a) gives a perspective view). Figures 1(c) and 1(d) show the reconstructed r_F and η for the case of a rigid linker, indicating excellent accuracy. In Figs. 1(e) and 1(f), we show the results for a and b with a flexible linker. Notice how well the true values are estimated. The key point is that we are able to determine the microscopic FRET parameters from the macroscopic ODT model with a realistic noise model, suggesting that the modality can be applied *in vivo*.

To emphasize the efficacy of our approach, consider the case in Fig. 3 of two spherical regions, each of radius 2 mm, containing FRET DA pairs connected by flexible linkers having differing parameters (a and b), simulating different micro-environments. Figures 3(a) and 3(c) show the true images of a and b, respectively, while Figures 3(b) and 3(d) show the reconstructed results. The η image in Fig. 3(e) is determined quite well in the reconstructed image of Fig. 3(f). We are thus able to accurately reconstruct the FRET distribution parameters, even if the FRET pairs are localized in two different regions with different distributions.

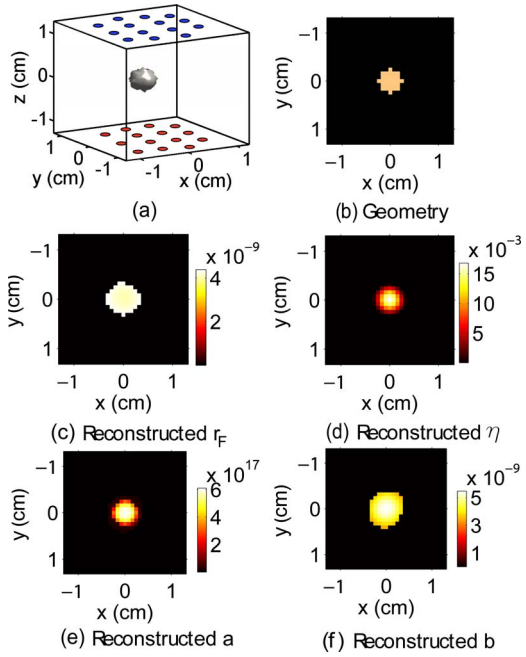

Fig. 1. (Color online) (a) The $r_F=4.2$ nm isosurface plot of the true image for a fixed linker. Also shown are the locations of the sources (top circles) and detectors (bottom circles) used to produce the simulated data. (b) Discretized spherical geometry with radius 2.5 mm (with $33\times33\times33$ image resolution). For a rigid linker with $r_F=4.2$ nm and $\eta=0.025$: (c) reconstructed r_F, (d) reconstructed η. For a flexible linker with $a=5.42\times10^{17}$ m^{-2} and $b=5.45$ nm, with the geometry in (b): (e) reconstructed a, (f) reconstructed b. The average detector SNR was 30 dB.

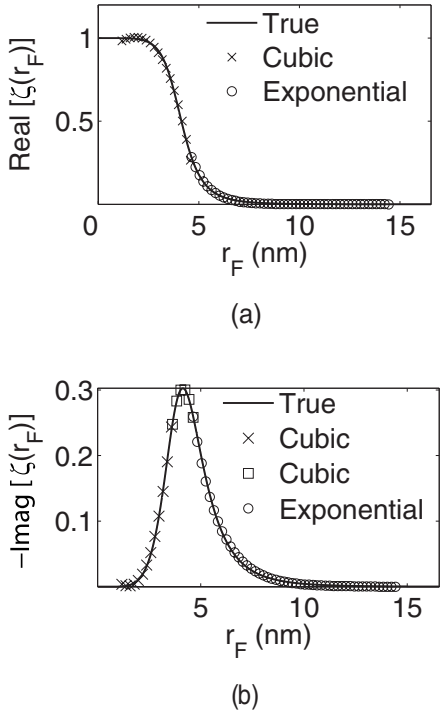

Fig. 2. Piecewise polynomial and exponential fitting of the real and imaginary parts of $\zeta(r_F)$ when $R_0=4.7$ nm and $\tau_D=3.8$ ns: (a) real part, and (b) imaginary part, for a modulation frequency of 80 MHz.

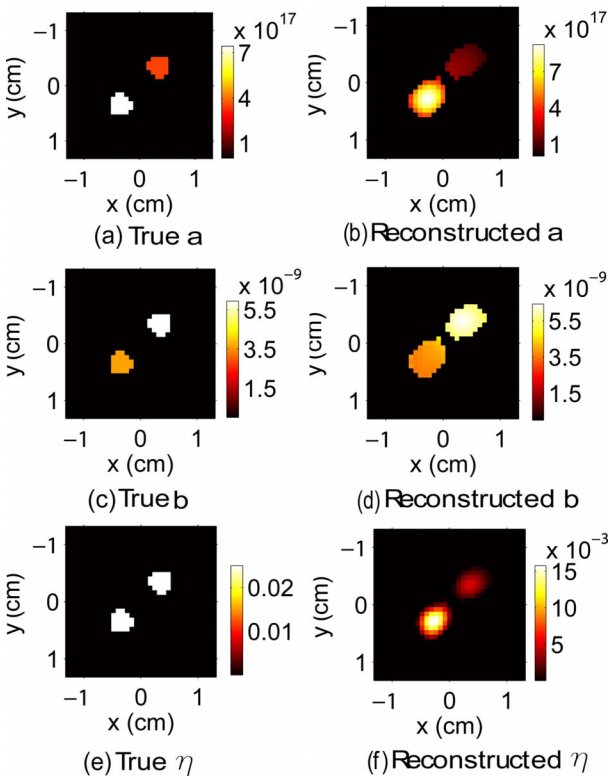

Fig. 3. (Color online) A phantom having two spheres, each of radius 2 mm, containing DA molecules connected by a flexible linker. (a) True image of a. For the top right sphere, $a=3.5\times10^{17}$ m^{-2}, and for bottom left sphere, $a=7.45\times10^{17}$ m^{-2}. (b) Reconstructed a. (c) True image of b. For top right sphere, $b=5.95$ nm, and for bottom left sphere, $b=3.65$ nm. (d) Reconstructed b. (e) True image of η. For top right and bottom left spheres, $\eta=0.025$. (f) Reconstructed η. The average detector SNR=30 dB.

5. EXPERIMENT

To verify the model and simulations, a simple experiment was performed. The goal was to reconstruct the DA distance for an ensemble of FRET DA molecules located inside a scattering medium. The FRET chemical was comprised of the donor, 4,4-difluoro-5, 7-dimethyl-4-bora-3a,4a -diaza- s-indacene-3-propionic acid (BODIPY-FL: excitation 488 nm, emission 520 nm), the acceptor, tetraethyl rhodamine, and a structurally rigid peptide linker whose chemical structure is described elsewhere [30]. Figure 4 shows a schematic of the ODT measurement system, with a 3 mW 488 nm argon-ion laser (Uniphase), an $x-y$ scanning mirror system, a Plexiglas box of size 8.8 cm (L)×8.8 cm (H)×3.4 cm (W), a cylindrical plastic vial (length 3 cm, inner-diameter 0.65 cm, outer-diameter 0.75 cm) to hold the FRET chemical, suspended from the lid of the Plexiglas box using an acrylic rod 1 mm in diameter and 1.5 cm in length, a 520 nm bandpass filter (Edmund Optics, 50.8 mm square) with FWHM 10 nm and peak transmission 45% [31], and a 105 mm, f/2.8 lens (AF micro Nikkor, Nikon) to focus the 4.8 cm×4.8 cm image of the scattering medium on a 512×512 pixel Peltier cooled CCD Camera (PI-MAX, Roper Scientific). The Plexiglas box was filled with a suspension of 0.4% (w/v) Intralipid (Sigma-Aldrich). The 0.4% Intralipid solution was prepared by dissolving 10 ml of 20% Intralipid in 500 ml of deionized water. The plastic vial contained 1 ml of 3 μM solution of the FRET chemical in Intralipid, prepared by mixing 100 μl of a 0.18 mM stock solution of the FRET chemical with 5.9 ml of 0.4% (w/v) Intralipid. The chemical was dissolved in Intralipid to maintain tissue-like scattering properties.

Using the $x-y$ scanning mirror system, the laser beam was scanned along the Plexiglas box surface to 19 prechosen source positions. For each source position, 100 frames with an exposure time of 150 msec each were taken with the camera and added together. For reconstruction, the 512×512 image was down-sampled to 16×16, giving 256 detectors in total. Each detector is one pixel, and the detector pixels were uniformly spaced. The laser was not modulated. We determined η experimentally, as described below, and use $\eta=15.6\times10^{-3}$ cm^{-1}. For the 0.4% Intralipid solution, we assume that all the absorption at $\lambda_x=488$ nm is due to water, thereby giving $\mu_{a_x}\approx2.5\times10^{-4}$ cm^{-1} and $\mu_{a_m}\approx3.2\times10^{-4}$ cm^{-1} [32]. Prior experiments with Intralipid lead to $D_x\approx0.051$ cm and $D_m\approx0.056$ cm [33].

Using the procedure outlined in Sections 3 and 5.C, the acquired data was calibrated and the images were reconstructed. For reconstruction, the scattering medium was discretized into a 33×33×17 uniform grid. In the calculation for r_F, we ignored the small contribution of

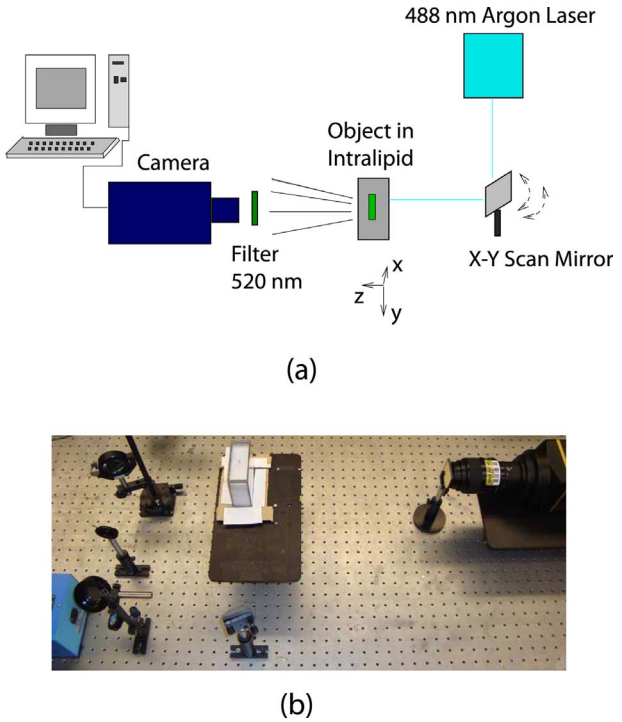

Fig. 4. (Color online) (a) and (b) Experimental setup: a 3 mW 488 nm argon-ion laser (Uniphase), an $x-y$ scanning mirror system, a Plexiglas box of size 8.8 cm (L)×8.8 cm (H)×3.4 cm (W), a cylindrical plastic vial (length 3 cm, inner-diameter 0.65 cm, outer-diameter 0.75 cm), to hold the FRET chemical, suspended from the lid of the Plexiglas box using an acrylic rod 1 mm in diameter and 1.5 cm in length, a 520 nm narrow bandpass filter (Edmund Optics) with FWHM 10 nm [31], and a 105 mm, f/2.8 lens (AF micro Nikkor, Nikon) to focus the 4.8 cm×4.8 cm image of the scattering medium on a 512×512 pixel Peltier cooled CCD Camera (PI-MAX, Roper Scientific).

rhodamine emission at 520 nm, when excited at 488 nm, as we found that compared to the emission of Bodipy-FL at 520 nm, rhodamine's signal was negligible. Also, due to the scattering medium, less than one μW was incident on the cuvette, which resulted in no observable photobleaching.

A. Determination of η

A solution of the donor BODIPY-FL and Intralipid was prepared by mixing 100 μl of a 10 μM stock solution of the donor BODIPY-FL with 3.9 ml of 0.4% (w/v) Intralipid, resulting in a concentration of $C_D=250$ nM. One ml of the donor-Intralipid solution was pipetted into a plastic vial (identical in size to the one described in the paper) and suspended inside the Plexiglas box containing 0.4% Intralipid. Using the same experimental setup as described above, the laser beam was scanned along the Plexiglas box surface to 26 pre-chosen source positions. For each source position, 100 frames with an exposure time of 150 msec each were acquired with the camera and added together. For reconstruction, the 512×512 image was down-sampled to a 16×16, thus making 256 detectors in total. Each detector is one pixel, and the detector pixels were uniformly spaced. For reconstruction, the scattering medium was discretized into a $33\times33\times17$ uniform grid. For the background optical properties, we assumed that for a 0.4% Intralipid solution, all the absorption was due to water, thereby giving $\mu_{a_x}\approx2.5\times10^{-4}$ cm^{-1}, $\mu_{a_m}\approx3.2\times10^{-4}$ cm^{-1} [32], $D_x\approx0.051$ cm and $D_m\approx0.056$ cm [33]. Using fluorescence optical diffusion tomography (FODT) [17], η was reconstructed. We note that related fluorescence imaging work has been termed fluorescence molecular tomography (FMT) [19]. Figure 5 shows three slices along the $x-y$ plane for the reconstructed η. The estimated η in the reconstructed image for the 250 nM solution was 13×10^{-4} cm^{-1}, giving $\eta=15.6\times10^{-3}$ cm^{-1} for the 3 μM solution used in the FRET imaging experiment.

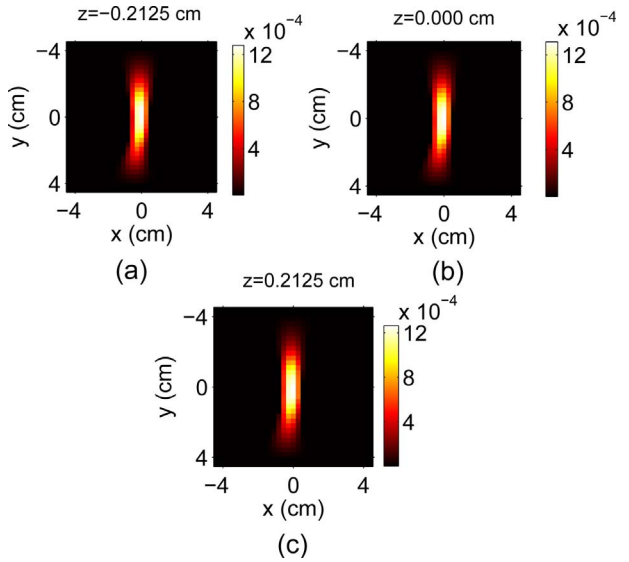

Fig. 5. (Color online) Slices along the $x-y$ plane of the reconstructed image of η for the plastic vial containing the donor mixed with Intralipid. (a) Slice at $z=-0.2125$ cm. (b) Slice at $z=0.0$ cm. (c) Slice at $z=0.2125$ cm. Reconstructed $\eta\approx0.0013$ cm^{-1}.

B. Computation of R_0

The Förster distance R_0 for the donor BODIPY-FL and acceptor rhodamine was calculated from [2]

$$R_0^6=\frac{9000\ln(10)\kappa^2\eta_D}{128\pi^5Nn^4}\int_{\lambda_{min}}^{\lambda_{max}}f_D(\lambda)\varepsilon_A(\lambda)\lambda^4d\lambda, \quad (17)$$

where κ^2 is the relative orientation of the donor and acceptor transition dipole moments, assumed to be $\kappa^2=2/3$, N is Avogadro's number, n is the solvent refractive index, which was assumed to be $n=1.33$ (the refractive index of water, because it is the main solvent), η_D is the donor quantum yield in the absence of the acceptor, which for BODIPY-FL is $\eta_D=0.9$ [34], $f_D(\lambda)$ is the normalized fluorescence spectrum of the donor, and $\varepsilon_A(\lambda)$ is the molar absorption coefficient of the acceptor at wavelength λ. The integral in (17) was calculated between $\lambda_{min}=475$ nm and $\lambda_{max}=649$ nm, giving $R_0=5.8$ nm.

C. Calibration for Experimental Data

Measurement calibration is necessary to account for source and detector coupling to the scattering medium. For accurate image reconstruction, a two step calibration procedure was followed. In the first step, a baseline measurement, y_{km}^{base}, for the kth source and mth detector, was made at the excitation wavelength (488 nm) with only Intralipid in the plastic vial and no filter in front of the CCD camera lens. Using the optical properties, i.e., D and μ_a for 0.4% Intralipid at 488 nm, described above, synthetic data y_{km}^{syn} was computed using a numerical solution to (3). Uncalibrated fluorescence data, y_{km}^{uncal}, obtained from the experiment described above, was calibrated using

$$y_{km}^{cal}=y_{km}^{uncal}\cdot\frac{y_{km}^{syn}}{y_{km}^{base}}, \quad (18)$$

where y_{km}^{cal} is the calibrated data for the kth source and mth detector. Thus, for our experiment, $Q=1$, $y_{F_1}=y^{cal}$ and $\omega_1=0$, because unmodulated light is used. As Eq. (18) does not fully characterize the source and wavelength-dependent detector arrangement, we found it necessary to explicitly introduce source and detector coupling coefficients into the inversion procedure [24].

D. Experiment Results

Figure 6 shows three slices along the $x-y$ plane of the true discretized location and shape of the plastic vial inside the scattering medium. Also shown is an isosurface image of the plastic vial plotted at a DA distance of $r_F=3.6$ nm, which was obtained from an another experiment (see Subsection 5.E, performed to verify that we accurately estimated the DA distance in the presence of scatter), in which we imaged the plastic vials in the absence of the scattering medium. Figure 7 shows the reconstructed image for the DA distance. As can be seen from the images, the reconstructed object is very close to Fig. 6 in terms of both object shape, object location and the reconstructed DA distance. Also shown in Fig. 7 is an isosurface plot for the reconstructed DA distance at $r_F=3.4$ nm.

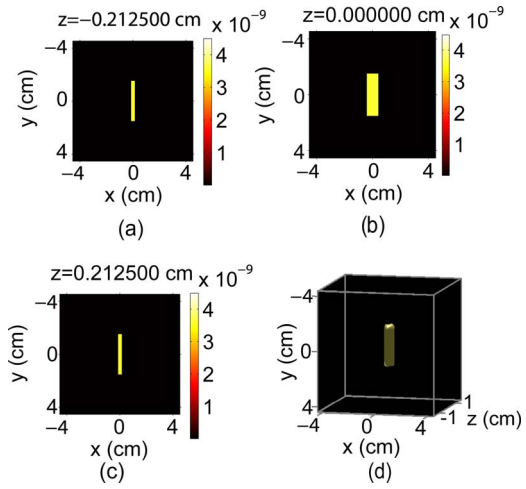

Fig. 6. (Color online) Slices along the $x-y$ plane of the true r_F, true location and shape of the plastic vial suspended inside the Intralipid scattering medium (see Fig. 3 for xyz axes orientation). (a) Slice at $z=-0.2125$ cm. (b) Slice at $z=0.0$ cm. (c) Slice at $z=0.2125$ cm. (d) Isosurface plot of the DA distance at $r_F=3.6$ nm, which is the distance estimated without the scattering medium (see Section 5.E).

E. Experiment to Verify Reconstruction of r_F

To verify whether the DA distance had been estimated accurately, we performed another experiment in which the plastic vials containing the 250 nM solution of donor and Intralipid and the 3 μM solution of the FRET chemical and Intralipid were imaged without the scattering medium with the same experimental setup shown in Fig. 4. Figure 8 shows the images for each vial. The detected power is proportional to the intensity in counts and is

$$P \propto \int I \, . \, dS, \tag{19}$$

where I is the intensity in counts and dS represents an area element. Using (19), the DA distance can be estimated from

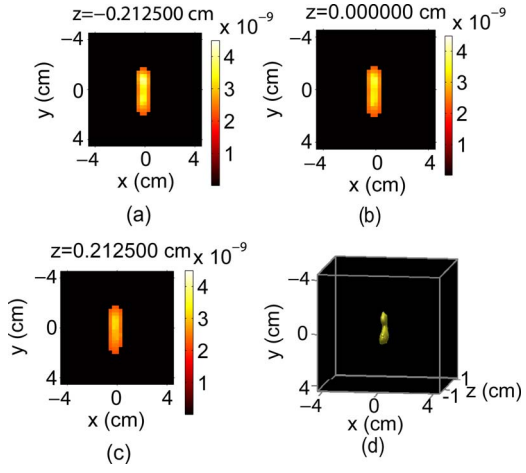

Fig. 7. (Color online) Slices along the $x-y$ plane of the reconstructed image of the DA distance. Expected $r_F=3.6$ nm. (a) Slice at $z=-0.2125$ cm. (b) Slice at $z=0.0$ cm. (c) Slice at $z=0.2125$ cm. (d) Isosurface plot of the reconstructed DA distance at $r_F=3.4$ nm.

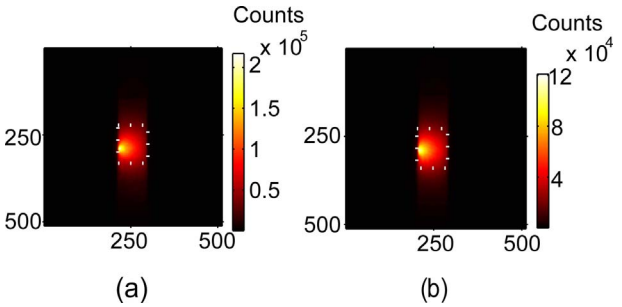

Fig. 8. (Color online) Acquired image of plastic vials without the scattering medium. (a) Image of vial containing donor Bodipy-FL mixed with Intralipid at concentration $C_D=250$ nM. The total detected power is assumed to be the integral of the intensity in the dotted rectangle, which gives $P_D=\gamma 7.3\times10^8$ W. (b) Image of the vial containing the FRET chemical mixed with Intralipid at concentration $C_{DA}=3$ μM. The detected power, using the intensity in the dotted rectangle, is $P_{DA}=\gamma 4.2\times10^8$ W. Using (20) and $R_0=5.8$ nm gives $r_F\approx3.6$ nm

$$\frac{P_D}{P_{DA}} = \frac{\eta_D C_D}{(\eta_D C_{DA})/[1+(R_0/r_F)^6]}, \tag{20}$$

where P_D and P_{DA} are the detected powers for the donor-only and FRET samples, respectively, C_D is the concentration of the donor, and C_{DA} is the concentration of the FRET chemical. This gives

$$r_F = R_0\left(\frac{C_{DA}P_D}{P_{DA}C_D} - 1\right)^{-1/6}, \tag{21}$$

which was calculated using the area highlighted in Fig. 8(a) and 8(b). For the images, $P_D\approx\gamma\cdot7.3\times10^8$ Watt and $P_{DA}\approx\gamma\cdot4.2\times10^8$ W, where γ is a proportionality constant (Watts/counts) which cancels out when P_D and P_{DA} are substituted in (20), and $R_0=5.8$ nm, yielding $r_F=3.6$ nm. This is very close to the reconstructed DA distance in the presence of scatter. In the calculation for r_F, we ignored the small contribution of rhodamine emission at 520 nm, when excited at 488 nm.

6. CONCLUSION

We have shown that it is possible to image the microscopic DA distance or distance distribution of a FRET chemical inside a scattering medium by incorporating FRET kinetics in an ODT framework. Through simulations, we showed the efficacy of our approach to distinguish macroscopic regions having differing ensemble parameters. This emulates a situation where multiple tumors or organs are imaged.

The macroscopic FRET regions used in the simulations and experiment are also representative of Alzheimer's, where the onset of senility occurs with a total senile plaque density of approximately 80 mm^{-2} [35] (716 mm^{-3}). Assuming a plaque dimension of 50 μm, this gives a minimum plaque volume of 3.5×10^{-3} cm^3 in a 1 cm^3 tissue volume, commensurate with the FRET volume length scale we considered. The simple tissue model experiment performed demonstrates that the microscopic DA distance can be determined in a heavily scattering

environment, leading to the conclusion that it should be possible to apply our approach *in vivo*. The resulting three-dimensional spatial maps of the DA distance could be used for quantitative deep tissue *in vivo* FRET imaging, thus expanding the study of disease through FRET. For example, using fluorescence lifetime imaging microscopy (FLIM) together with FRET, Bacskai *et al.* [36] showed a distribution of lifetimes within individual senile plaques (characteristic features of Alzheimer's formed by large deposits of amyloid—β peptides), which implied that amyloid—β has different conformations within the plaque. Although the size of an individual plaque (order of 10 μm) is smaller than the resolution of ODT, because senile plaques exist as an aggregate, with appropriate DA labeling, an *in vivo* image of a distance distribution representative of amyloid—β could be extracted, as we have described. Deep tissue FRET imaging should also facilitate the study of cancers related to protein misfolding [8,10,11,37]. Our results suggest that, with similar SNRs (integration times), we should be able to detect smaller FRET regions or lower concentrations. A more sophisticated experiment involving small animals like mice would further establish the efficacy of our approach.

ACKNOWLEDGMENTS

We acknowledge funding from the National Science Foundation under award CCR-0431024.

REFERENCES

1. T. Förster, "Zwischenmolekulare energiewanderung und fluoreszenze," Ann. Phys. **2**, 55 (1948).
2. J. R. Lakowicz, *Principles of Fluorescence Spectroscopy*, 2nd ed. (Kluwer Academic, 1999).
3. R. D. Mitra, C. M. Silva, and D. C. Youvan, "Fluorescence resonance energy transfer between blue-emitting and red-shifted excitation derivatives of green fluorescent protein," Gene **173**, 13–17 (1996).
4. Y. Suzuki, T. Yasunaga, R. Ohkura, T. Wakabayashi, and K. Sutoh, "Swing of the lever arm of a myosin motor at the isomerization and phosphate-release steps," Nature **396**, 380–383 (1998).
5. M. Sato, T. Ozawa, K. Inukai, T. Asano, and Y. Umezawa, "Fluorescent indicators for imaging protein phosphorylation in single living cells," Nat. Biotechnol. **20**, 287–294 (2002).
6. A. Miyawaki, J. Llopis, R. Heim, J. McCaffery, J. Adams, M. Ikura, and R. Tsien, "Fluorescent indicators for, Ca^{2+} based on green fluorescent proteins and calmodulin," Nature **388**, 881–887 (1997).
7. N. Mahajan, K. Linder, G. Berry, G. Gordon, R. Heim, and B. Herman, "Bcl-2 and bax interactions in mitochondria probed with green fluorescence protein and fluorescence resonance energy transfer," Nat. Biotechnol. **16**, 547–552 (1998).
8. E. Haas, "The study of protein folding and dynamics by determination of intramolecular distance distributions and their fluctuations using ensemble and single-molecule FRET measurement," Chem. Phys. **6**, 858–870 (2005).
9. K. Truong and M. Ikura, "The use of FRET imaging technology to detect protein-protein interactions and protein conformational changes *in vivo*," Curr. Op. Struct. Biol. **11**, 573–578 (2001).
10. C. Dobson, "The structural basis of protein folding and its links with human disease," Phil. Trans. R. Soc. Lond. B **356**, 133–145 (2001).
11. A. Bullock and A. Fersht, "Rescuing the function of mutant p53," Nat. Rev. Cancer **1**, 1 (2001).
12. J. Mills, J. Stone, D. Rubin, D. Melon, D. Okonkwo, and A. P. G. Helm, "Illuminating protein interactions in tissue using confocal and two-photon excitation fluorescent resonance energy transfer microscopy," J. Biomed. Opt. **8**, 347–356 (2003).
13. R. Yasuda, C. Harvey, H. Zhong, A. Sobczyk, L. Aelst, and K. Svoboda, "Supersenstive ras activation in dendrites and spines revealed by two-photon fluorescence lifetime imaging," Nature Neurosci. **9**, 283–291 (2006).
14. D. Stockholm, M. Bartoli, G. Sillon, N. Bourg, J. Davoust, and I. Richard, "Imaging calpain protease activity by multiphoton FRET in living mice," J. Mol. Biol. **346**, 215–222 (2005).
15. A. B. Milstein, S. Oh, J. S. Reynolds, K. J. Webb, C. A. Bouman, and R. P. Millane, "Three-dimensional Bayesian optical diffusion tomography with experimental data," Opt. Lett. **27**, 95–97 (2002).
16. A. P. Gibson, J. C. Hebden, and S. R. Arridge, "Recent advances in diffuse optical imaging," Phys. Med. Biol. **50**, R1–R43 (2005).
17. A. B. Milstein, S. Oh, K. J. Webb, C. A. Bouman, Q. Zhang, D. A. Boas, and R. P. Millane, "Fluorescence optical diffusion tomography," Appl. Opt. **42**, 3081–3094 (2003).
18. S. Tyagi and F. Kramer, "Molecular beacons: Probes that fluoresce upon hybridization," Nat. Biotechnol. **14**, 303–308 (1996).
19. V. Ntziachristos, C. Tung, C. Bremer, and R. Weissleder, "Fluorescence molecular tomography resolves protease activity in vivo," Nat. Med. **8**, 757–760 (2002).
20. S. Bernacchi and Y. Mely, "Exciton interaction in molecular beacons: a sensitive sensor for short range modifications of the nucleic acid structure," Nucleic Acids Res. **29**, e62 (2001).
21. S. Marras, F. Kramer, and S. Tyagi, "Efficiencies of fluorescence resonance energy transfer and contact-mediated quenching in oligonucleotide probes," Nucleic Acids Res. **30**, e122 (2002).
22. A. Milstein, J. Stott, S. Oh, D. Boas, R. Millane, C. Bouman, and K. Webb, "Fluorescence optical diffusion tomography using multiple-frequency data," J. Opt. Soc. Am. A **21**, 1035–1049 (2004).
23. J. C. Ye, K. J. Webb, C. A. Bouman, and R. P. Millane, "Optical diffusion tomography using iterative coordinate descent optimization in a Bayesian framework," J. Opt. Soc. Am. A **16**, 2400–2412 (1999).
24. S. Oh, A. B. Milstein, R. P. Millane, C. A. Bouman, and K. J. Webb, "Source-detector calibration in three-dimensional Bayesian optical diffusion tomography," J. Opt. Soc. Am. A **19**, 1983–1993 (2002).
25. J. C. Ye, C. A. Bouman, K. J. Webb, and R. P. Millane, "Nonlinear multigrid algorithms for Bayesian optical diffusion tomography," IEEE Trans. Image Process. **10**, 909–922 (2001).
26. P. Schwille, S. Kummer, A. Heikal, W. Moerner, and W. Webb, "Fluorescence correlation spectroscopy reveals fast optical excitation-driven intramolecular dynamics of yellow fluorescent proteins," Proc. Natl. Acad. Sci. U.S.A. **97**, 151–156 (2000).
27. www.microscopyu.com/tutorials/java/fluorescence/fpfret/index.html.
28. J. C. Adams, "Mudpack: Multigrid portable fortran software for the efficient solution of linear elliptic partial differential equations," Appl. Math. Comput. **34**, 113–146 (1989).
29. J. C. Adams, *Multigrid Software for Elliptic Partial Differential Equations* (National Center for Atmospheric Research, Boulder, Colorado, 1991).
30. J. Yang, H. Chen, I. Vlahov, J. Cheng, and P. Low, "Evaluation of disulfide reduction during receptor-mediated endocytosis by using FRET imaging," Proc. Natl. Acad. Sci. U.S.A. **103**, 13872–13877 (2006).
31. http://www.edmundoptics.com/onlinecatalog/displayproduct.cfm?productid=1903.
32. G. Hale and M. Querry, "Optical constants of water in the

200 nm to 200 μm wavelength region," Appl. Opt. **12**, 555–563 (1973).
33. R. Michels, F. Foschum, and A. Kienle, "Optical properties of fat emulsions," Opt. Express **16**, 5907–5925 (2008).
34. http://probes.invitrogen.com/handbook/sections/0104.html.
35. L. Berg, D. W. McKeel, J. P. Miller, M. Storandt, E. H. Rubin, J. C. Morris, J. Baty, M. Coats, J. Norton, A. M. Goate, J. L. Price, M. Gearing, S. S. Mirra, and A. M. Saunders, "Clinicopatholigic studies in cognitively healthy aging and Alzheimer disease," Arch. Neurol. **55**, 326–355 (1998).
36. B. Bacskai, J. Skoch, G. Hickey, R. Allen, and B. Hyman, "Fluorescence resonance energy transfer determinations using multiphoton fluorescence lifetime imaging microscopy to characterize amyloid-beta plaques," J. Biomed. Opt. **8**, 368–375 (2003).
37. C. Dobson, "Protein folding and misfolding," Nature **426**, 884–890 (2003).